RSC Advances

ROYAL SOCIETY OF CHEMISTRY

PAPER

View Article Online
View Journal | View Issue

Cite this: *RSC Adv.*, 2025, **15**, 9644

Different conjugates of Fe_3O_4 nanoparticles, drug, and dye: optical and magnetic properties for *in vivo* bimodal imaging

Thi Thu Huong Le,[a] Ke Son Phan,[b] Bich Thuy Doan,[c] Thi Thu Trang Mai,[b] Ha Bao Hung Bui,[b] Hong Nam Pham,[b] Thi Dieu Thuy Ung,[b] Yiqian Wang,[c] Ngoc Quyen Tran,[d] Le Hang Dang[d] and Phuong Thu Ha *[b]

Bioimaging is very important in medicine, especially in cancer diagnosis and treatment. In this study, we determined the impact of different components on the optical and magnetic properties of various conjugates. The three components, *i.e.*, Fe_3O_4 nanoparticles (NPs), drug (doxorubicin – Dox), and dye (Cyanine 5.5 – Cy 5.5), were incorporated to form the four conjugates of A1 (Fe_3O_4–Cy 5.5), A2 (Fe_3O_4–Dox), A3 (Fe_3O_4–Cy 5.5–Dox), and A4 (Cy 5.5–Dox). The conjugates were characterized by DLS, UV-Vis spectra, fluorescence spectra, VSM, XRD, and TEM methods. After that, *in vitro* near-infrared (NIR) fluorescence imaging and magnetic resonance imaging (MRI) experiments were carried out to determine the conjugate suitable for bimodal imaging. The results show that A3 exhibits the highest quantum yield and radiance ratio and also has the highest ratio of r_2/r_1. The *in vivo* MRI and NIR fluorescent imaging results of CT26-bearing mice injected with A3 conjugates prove that the conjugate has potential in bimodal cancer imaging applications.

Received 6th November 2024
Accepted 23rd March 2025

DOI: 10.1039/d4ra07910h

rsc.li/rsc-advances

1 Introduction

Cancer has become one of the leading threats to human health in today's society, leading to high morbidity and mortality rates worldwide. According to a report from the International Agency for Research on Cancer (IARC), there were nearly 20 million new cancer cases and 9.7 million cancer deaths in 2022. The report also estimates that about 1 in 5 men or women will develop cancer during their lifetime, while about 1 in 9 men or 1 in 12 women will die from cancer.[1] Therefore, developing new methods for diagnosing and treating cancer, which directly target cancer cells without affecting healthy cells, is of great interest to many research groups.

Tumor imaging plays an important role in the advancement of cancer diagnosis because it allows non-invasive measurement of the biodistribution and pharmacokinetics of drugs, allowing us to determine where the drugs have gone, whether they have reached the tumor, how long they stay in the body, and how they are cleared.[2] Magnetic resonance imaging (MRI) and fluorescence imaging attract much attention among various imaging techniques. Compared to other techniques, MRI can provide the best spatial resolution. However, its specificity is not high (which can cause a false positive rate of 10% for breast cancer). Therefore, it is necessary to use MRI contrast-enhancing agents such as superparamagnetic Fe_3O_4 nanoparticles (NPs).[2] Besides, fluorescence imaging provides non-ionizing, portable, low-cost radiation with some advantages, including real-time imaging, higher resolution, and high sensitivity. Recently, near-infrared (NIR) fluorescence probes have been rapidly developed due to their important advantages over conventional optical imaging, including deeper tissue penetration, lower tissue absorption, and higher signal-to-background ratio.[3] However, although NIR imaging is highly sensitive for diagnosing tumor tissue, it cannot differentiate between anatomical structures and has a limited penetration depth (less than 10 mm).[4] Thus, no single imaging modality is perfect or sufficient to capture all the necessary information, so combining them will help to obtain more comprehensive information about the tumor and avoid the shortcomings of each individual technique.

Fe_3O_4 nanoparticles (MNPs) have shown great promise for diagnostic and therapeutic applications. Fe_3O_4 nanoparticles smaller than 20 nm are typically in a superparamagnetic state at room temperature, *i.e.*, their magnetism can reach saturation value when exposed to an external magnetic field. In the absence of an external magnetic field, their magnetic moments align randomly, and their magnetization becomes zero. Due to

[a]*Faculty of Natural Resources and Environment, Vietnam National University of Agriculture, Hanoi, Vietnam*
[b]*Institute of Materials Science, Vietnam Academy of Science and Technology, Hanoi, Vietnam. E-mail: thuhp@ims.vast.ac.vn*
[c]*The Institute I-CLeHS Institute of Chemistry for Life and Health Sciences, ENSCP Chimie ParisTech, PSL Université, CNRS UMR 8060, Paris, France*
[d]*Institute of Advanced Technology, Vietnam Academy of Science and Technology, Ho Chi Minh City, Vietnam*

their unique magnetic properties and size comparable to biologically important objects, Fe_3O_4 nanoparticles are being studied for a variety of biomedical applications, such as drug delivery, MRI contrast enhancement, and hyperthermia.[5] A small amount of these NPs can be used for MRI tumor detection because when placed in a magnetic field, they will disturb the magnetic field, causing water protons to relax faster, thus allowing for increased MRI contrast.[6] Multifunctional nanosystems based on Fe_3O_4 NPs were also reported.[7,8]

Cyanine compounds have many important photophysical and photochemical properties. At the same time, they have high biocompatibility and low toxicity, which makes them used in many applications in biomedicine, diagnostic imaging, and biochemistry. Recent studies have also shown that combining these advantages of Cyanine with nanoparticles allows the creation of many conjugates with improved desired functions.[9] A 2014 study fabricated a conjugate system containing Fe/Fe_3O_4 nanoparticles and Cyanine 5.5 (covalently bound to the surface of the particles) to measure the activity of cancer-related proteases in biological samples.[10] The results of the study showed that the measurement using the nanosystem was highly sensitive (as low concentration as 1×10^{-16} mol L^{-1} for 12 proteases), selective, and rapid (time required: 60 min). Cyanine 5.5 (Cy5.5) was conjugated with chitosan glycol to form spherical nanoparticles (containing 5.8% Cy5.5) with an average size of about 260 nm, stable in an aqueous medium. Thanks to the near-infrared (NIR) fluorescence of Cy5.5, the study determined that the maximum accumulation time in the tumor of the nanoparticles was from 48 to 96 hours, and the main organ that helped eliminate the nanoparticles from the body was the kidney.[11] Fe_3O_4 nanoparticles surface functionalized with branched polyethyleneimine (b-PEI) and conjugated with Cy 5.5 produced a red signal on confocal fluorescence microscopy images, allowing to determine intracellular uptake of the nanoparticles by cells and showing the potential application in *in vivo* fluorescence imaging.[12]

Doxorubicin (Dox) is the most widely used drug in the treatment of many types of cancer in different organs (lung, stomach, breast, ovary, …). However, its high toxicity to healthy cells and serious side effects limit its applications in clinical treatment.[13] To overcome these disadvantages, various DOX carrier systems, especially nanostructured drug carriers, have been studied to reduce the side effects of DOX while improving its therapeutic efficacy.[14–17] Although Dox can absorb at 488 nm and emit fluorescence at 591 nm, its quantum yield is only 9% compared to that of rhodamine 6G (95%).[18] Therefore, *in vivo* imaging usually requires other fluorophores like FCR-675 amine[19] or DiR.[20]

Alginate, a natural polysaccharide extracted from brown algae, has various applications in the pharmaceutical and biomedical fields thanks to its biocompatibility and biodegradability. In addition, its stable and viscous aqueous solution makes alginate suitable for being used in different drug delivery nanosystems.[21,22] In our previous studies, a nanosystem of Cyanine 5.5, Dox, and Fe_3O_4 was prepared based on synthetic PLA-TPGS copolymer. The *in vitro* toxicity on cancer cell lines and some *in vitro* optical and MRI imaging experiments of the system were carried out.[23] The *in vivo* biodistribution of the nanosystem was also determined in normal mice.[24] In this work, various conjugates (A1: Fe_3O_4–Cy5.5; A2: Fe_3O_4–Dox; A3: Fe_3O_4–Cy5.5–Dox; A4: Cy5.5–Dox) of the three components were prepared based on a natural polymer (alginate). The conjugates were fully examined for their optical and magnetic properties including quantum yield and magnetic inductive heating performance. The optimized conjugate was chosen for *in vivo* bimodal MRI and NIR-fluorescence imaging in tumor-bearing mice.

2 Materials and method

2.1. Materials

$FeCl_3 \cdot 6H_2O$ ≥99%, $FeCl_2 \cdot 4H_2O$ ≥9%, *N*-(3-dimethylaminopropyl)-*N*′-ethylcarbodiimide hydrochloride (EDC), *N*-hydroxysuccinimide (NHS), and doxorubicin hydrochloride (Dox), NaOH ≥99%, HCl (37%), NH_3 solution (26%), 4-(dicyanomethylene)-2-methyl-6-(*p*-dimethylaminos-tyryl)-4*H*-pyran (DCM), ethanol, alginate (Alg) with a molecular weight of 10 000 were provided by Sigma Aldrich. Cyanine 5.5 NHS ester ($C_{44}H_{46}N_3BF_4O_4$) was purchased from Lumiprobe GmbH (Europe). (3-Aminopropyl)triethoxysilane (APTES), and phosphate buffered solution (PBS, pH 7.4) were purchased from Merck. All chemicals were used without further purification. Distilled water was used for all experiments.

2.2. Methods

2.2.1 Synthesis of the nanoconjugates. Fe_3O_4 nanoparticles were first prepared using $FeCl_3$, $FeCl_2$, and NH_3 solution according to a published procedure.[25,26] After the purification, Fe_3O_4 NPs were dispersed in an aqueous alginate solution (2 mg mL^{-1}) by ultrasonic vibration to obtain 4 mg mL^{-1} Fe_3O_4 dispersion. In the next step, Fe_3O_4 NPs were surface functionalized with NH_2 groups by adding 100 μL APTES into 10 mL of the Fe_3O_4 suspension, and the mixture was allowed to react for 3 h at 60 °C. A1 (Fe_3O_4–Cyanine 5.5) was obtained by the reaction between Cyanine 5.5 NHS ester and the NH_2-modified Fe_3O_4 NPs with the catalysts of EDC and NHS for 24 h. A3 (Fe_3O_4–Cyanine 5.5–Dox) was derived from A1 by further adding Dox to the reaction mixture for another 6 h. For the synthesis of A2 (Fe_3O_4–Dox), Dox was added to the alginate–Fe_3O_4 dispersion in the presence of EDC and NHS. The mixture was finished after 6 h. A4 (Cyanine 5.5–Dox) was a combination of Cyanine 5.5 and Dox with the alginate solution. The detailed composition of the samples is presented in Table 1. The samples were then purified by dialysis against deionized water for 12 h (molecular weight cutoff 3.5 kDa) to remove unreacted substances and then freeze-dried for further use.

2.2.2 Characterizations. The samples were subjected to Fourier transform infrared (FT-IR) absorption spectra in the wave number range of 400–4000 cm^{-1} using KBr pellets on a SHIMADZU spectrometer. UV-Vis spectra were recorded by a UV-Vis Aligent 8453. Fluorescence emission spectra were obtained using an iHR550 spectrometer (Horiba) with a 355 nm diode laser excitation. The samples with the initial

Table 1 Composition of the samples

No.	Sample		Concentration (mg mL^{-1})		
			Fe_3O_4	Cy 5.5	Dox
1	A1	Fe_3O_4–Cy 5.5	2	0.05	0
2	A2	Fe_3O_4–Dox	2	0	0.25
3	A3	Fe_3O_4–Cy 5.5–Dox	2	0.05	0.25
4	A4	Cy 5.5–Dox	0	0.05	0.25

concentration (C_0, presented in Table 1) were diluted 10 times with distilled water to record their UV-Vis and fluorescence spectra.

To calculate their quantum yield (QY), the samples were prepared as aqueous solutions with the absorbance values at 355 nm below 0.1. DCM was also dissolved in ethanol to obtain a reference solution with a similar absorbance value. The fluorescence spectra of the samples and the reference solution were recorded in the same conditions to determine the integrated

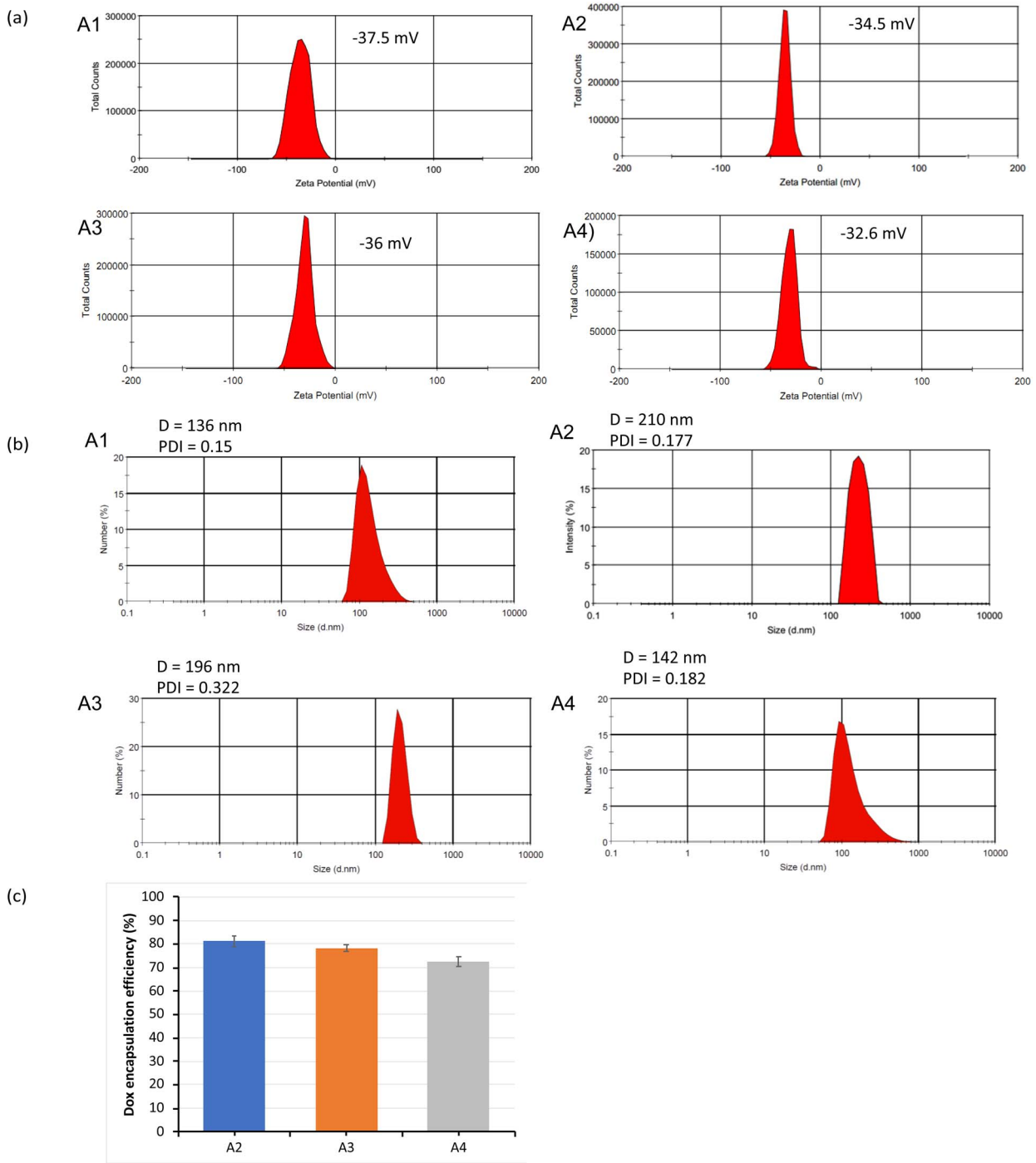

Fig. 1 Hydrodynamic size (a), zeta potential (b), and Dox encapsulation efficiency (c) of the conjugates.

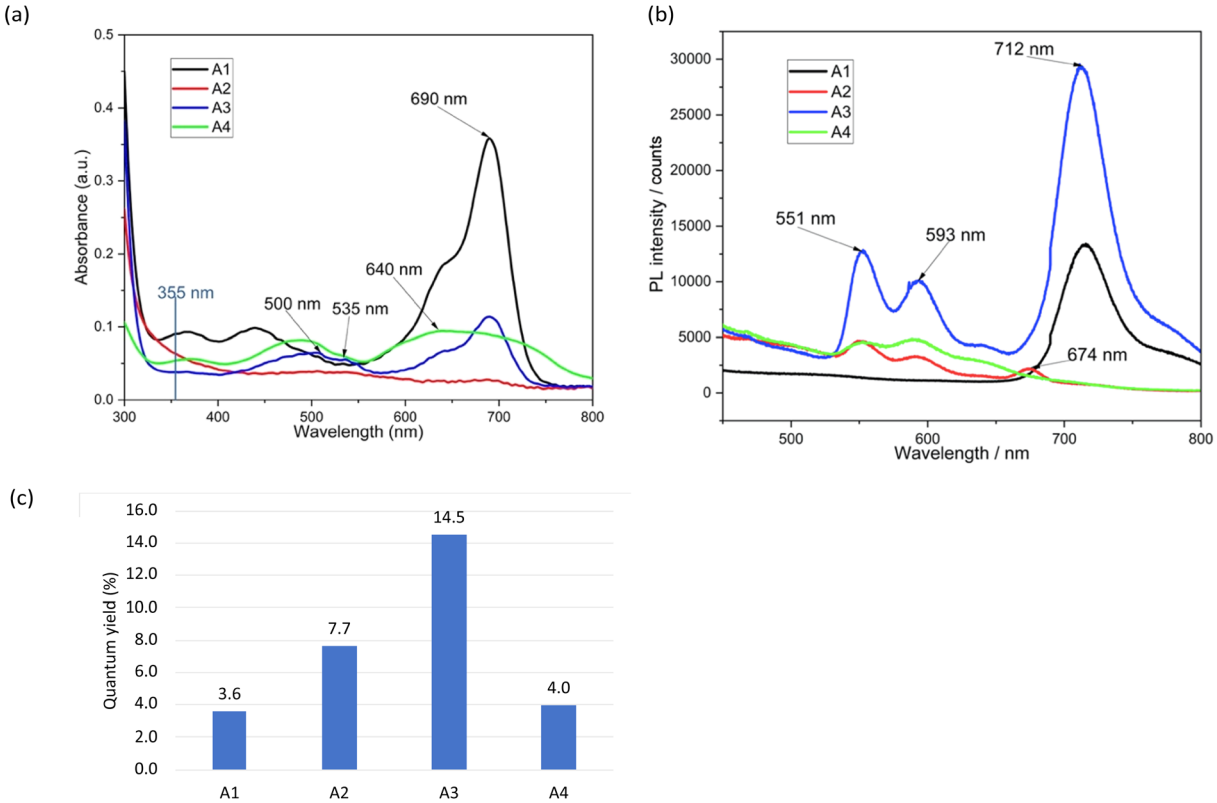

Fig. 2 UV-Vis spectra (a) and PL spectra (b) of the conjugates at $C_0/10$ concentration and quantum yield of the samples (c).

fluorescence intensity of the emitted light. QY of the samples were calculated by eqn (1):

$$Q_s = Q_r\left(\frac{A_r}{A_s}\right)\left(\frac{E_s}{E_r}\right)\left(\frac{n_s}{n_r}\right)^2 \quad (1)$$

In which Q is the fluorescence quantum yield, A is the absorbance of the solution, n is the refractive index of the solvent and E is the intergrated fluorescence intensity. The subscript "r" and "s" refer to the reference and sample respectively. In our case, $Q_r = Q_{DCM} = 43.5\%$, $n_s = n_{water} = 1.33$ and $n_r = n_{ethanol} = 1.36$.[27,28]

The hydrodynamic size and zeta potential of the nanosystems in water were determined by dynamic light scattering using a Malvern Nano-ZS ZEN 3600 instrument. X-ray

Table 2 The radiance ratio of the conjugates and control (agar) at different excitation/emission wavelengths

	λ_{ex} = 487 nm				λ_{ex} = 512 nm				λ_{ex} = 537 nm		
	λ_{em} = 547 nm	λ_{em} = 572 nm	λ_{em} = 597 nm	λ_{em} = 622 nm	λ_{em} = 547 nm	λ_{em} = 572 nm	λ_{em} = 597 nm	λ_{em} = 622 nm	λ_{em} = 572 nm	λ_{em} = 597 nm	λ_{em} = 622 nm
A1	0.52	0.43	0.34	0.23	0.80	0.61	0.62	0.41	0.69	0.95	0.76
A2	0.63	0.86	1.06	0.89	0.72	1.01	1.25	1.04	1.93	**2.38**	1.94
A3	1.44	1.54	1.95	1.22	1.34	2.47	3.08	1.90	5.58	6.74	4.13
A4	2.37	3.15	4.0	2.93	4.1	5.7	7.69	5.45	6.6	8.8	6.22

	λ_{ex} = 637 nm				λ_{ex} = 662 nm				λ_{ex} = 687 nm		
	λ_{em} = 697 nm	λ_{em} = 722 nm	λ_{em} = 747 nm	λ_{em} = 772 nm	λ_{em} = 697 nm	λ_{em} = 722 nm	λ_{em} = 747 nm	λ_{em} = 772 nm	λ_{em} = 722 nm	λ_{em} = 747 nm	λ_{em} = 772 nm
A1	19.2	30.1	22.3	21.2	41.6	68.0	51.5	50	75.0	73.3	**84.1**
A2	0.54	0.59	0.60	0.59	0.53	0.56	0.58	0.58	0.62	0.57	0.57
A3	73.2	178.8	99.9	121.6	62.5	229.8	124.8	67.3	**236.7**	108.4	49.2
A4	1.94	2.31	2.06	1.97	7.75	7.77	5.96	5.62	8.62	**9.63**	8.83

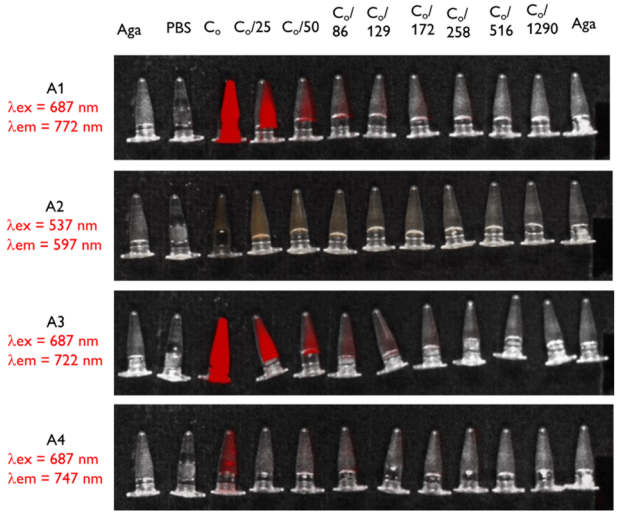

Fig. 3 *In vitro* fluorescence images of the conjugates at different concentrations (C_0, C_0/25, C_0/50, C_0/86, C_0/129, C_0/172, C_0/258, C_0/516, C_0/1290) compared to agar (Aga) at their optimal excitation/emission wavelength.

diffraction (XRD) method (SIEMENS-D5000) was used to determine the crystal structure of the Fe_3O_4-containing nanosystems. The magnetic properties of the systems were measured using a homemade vibrating sample magnetometer (VSM) at room temperature. The morphology of the nanoparticles was determined by transmission electron microscopy (TEM) on a JEOL JEM-1010.

Dox entrapment efficiency (EE%) of A2, A3, and A4 was determined by UV-Vis spectra at 485 nm based on a calibration curve of standard Dox solutions. EE% was calculated by the following formula:

$$\text{EE}\ (\%) = \frac{\text{the weight of loaded Dox}}{\text{the initial weight of free Dox}} \times 100\ (\%) \quad (2)$$

Magnetic inductive heating curves of A1, A2, and A3 were recorded on a commercial generator (Model UHF-20A) with the magnetic field amplitude varying from 100 to 250 Oe and at the frequency of 450 kHz. An optical thermometer (GaAs sensor, Opsens) was used to measure the sample temperature in the range of 0 to 250 °C.

Specific absorption rate (SAR) and intrinsic loss power (ILP) of the samples were calculated by eqn (3) and (4):

$$\text{SAR} = \frac{m_{\text{sample}}}{m_{Fe_3O_4}} \times C \times \frac{dT}{dt} \quad (3)$$

$$\text{ILP} = \frac{\text{SAR}}{H^2 \cdot f} \quad (4)$$

In which m_{sample} is the mass of the sample, $m_{Fe_3O_4}$ is the mass of Fe_3O_4 NPs present in the sample, and C is the specific heat of the aqueous medium ($C = 4.18$ J per g per °C), $\frac{dT}{dt}$ is the slope of the heating curve, H and f are the magnetic field and frequency of the applied field.

2.2.3 *In vitro* optical imaging. A photon imager (PHOTON IMAGER OPTIMA system, Biospace lab, France) was used to perform *in vitro* fluorescent imaging of the sample solutions with the control of the agar sample. A filter set with several excitation wavelengths from 487 to 687 nm and several emission wavelengths from 547 to 772 nm was used for the experiments. The region of interest was delineated in the obtained images and the mean radiance (the number of photons per second that are leaving a square centimeter of the tube and radiating into a solid angle of one steradian – ph s^{-1} cm^{-2} sr^{-1}) was calculated by the M3 vision software (BioSpace Lab, France). The optimal excitation/emission wavelengths are the wavelengths at which the ratio between the radiance of the sample and the radiance of the control (agar) reaches maximum. Each sample was imaged at the initial concentration (C_0) presented in Table 1 and various diluted concentrations (C_0/25, C_0/50, C_0/86, C_0/129, C_0/172, C_0/258, C_0/516, C_0/1290).

2.2.4 *In vitro* MRI. Relaxivity of A1, A2, and A3 NPs at different concentrations of iron (0, 0.02, 0.1, 0.15 and 0.2 mM in agarose gel 1% in PBS) was determined by recording T_2 and T_1 maps with a 7 T MR imaging vertical spectrometer fitted with an ultra-shielded refrigerated magnet (300WB, Bruker, Avance II, Wissembourg, France), and equipped with a nominative 200 mT min^{-1} actively shielded gradient. Then, relaxivity (r_1 or r_2) was calculated through the curve fitting of the relaxation rate ($1/T_1$ or $1/T_2$, s^{-1}) *versus* the iron concentration (mM).

2.2.5 *In vivo* imaging experiments. All *in vivo* experiments were performed in mice according to the institution's guidelines and approved by the institutional ethics committee (CEEA34.JS.142.1). Female Balb/C mice (Janvier, St. Genest de Lisle, France) implanted with CT26 tumors (one tumor on each flank) were used in the imaging experiments.

2.2.6 *In vivo* fluorescent imaging. 6 mice were anesthetized with a ketamine/xylazine mixture (80 mg kg^{-1}/10 mg kg^{-1}), and then 150 μL of A3 (25.8 mM of iron or 0.065 mM Cyanine 5.5) was injected into the tail vein of three mice using a 26G needle. The 3 remaining mice were used as control. A compression point at the injection site was performed for 10 seconds to avoid bleeding. At specific times after injection, *i.e.*, at 2, 5, 10, 30 min,

Table 3 Magnetic properties of A1, A2 and A3

Sample	M_s (emu g^{-1})	H_c (Oe)	dT/dt (°C s^{-1}) (100 Oe)	ΔT_{1500s} (100 Oe)	SAR (W g^{-1}) (100 Oe)	ILP (nH m^2 kg^{-1})	r_1 (s^{-1} mM^{-1})	r_2 (s^{-1} mM^{-1})	r_2/r_1
A1	63.6	6.7	0.12	43.7	250.8	8.7	0.6671	133.08	199.49
A2	59.9	5.0	0.11	38.6	229.9	8.0	0.9715	150.97	155.40
A3	45.9	8.3	0.07	25.3	146.3	5.1	0.2852	87.884	308.15

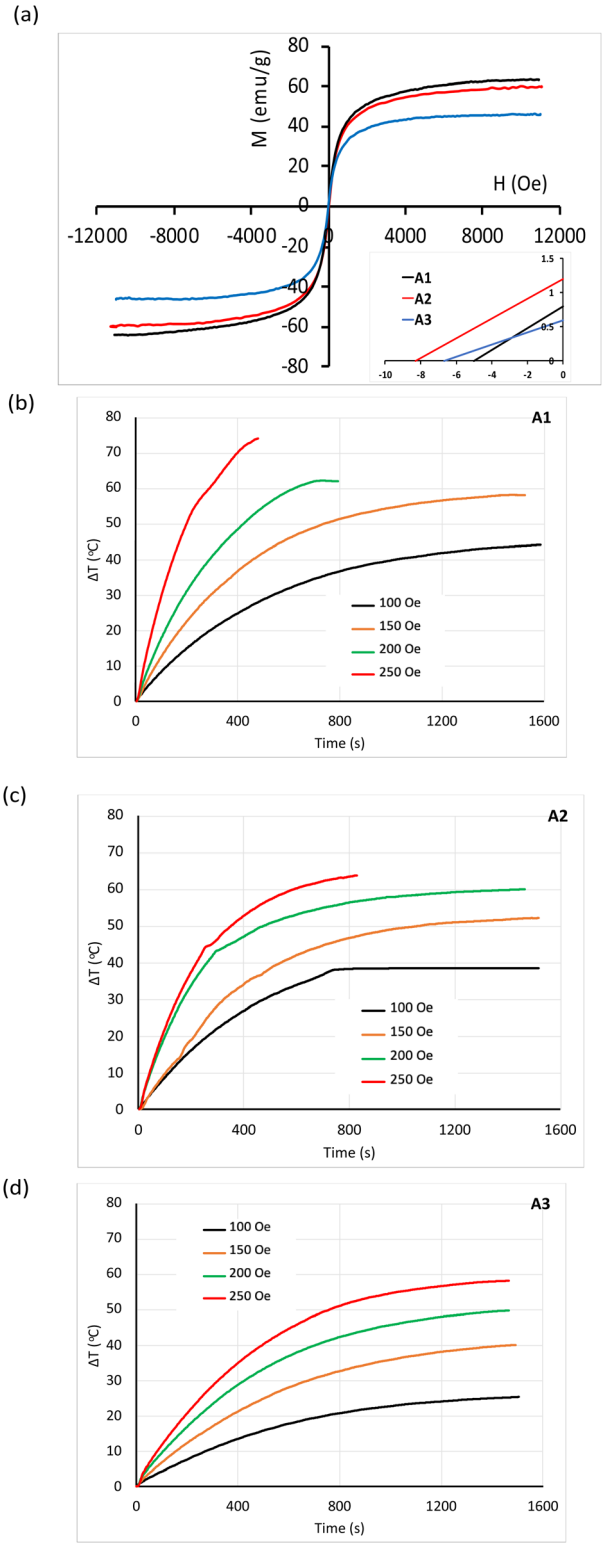

Fig. 4 Magnetic hysteresis loops (a) and magnetic heating curves of A1 (b), A2 (c), and A3 (d) conjugates.

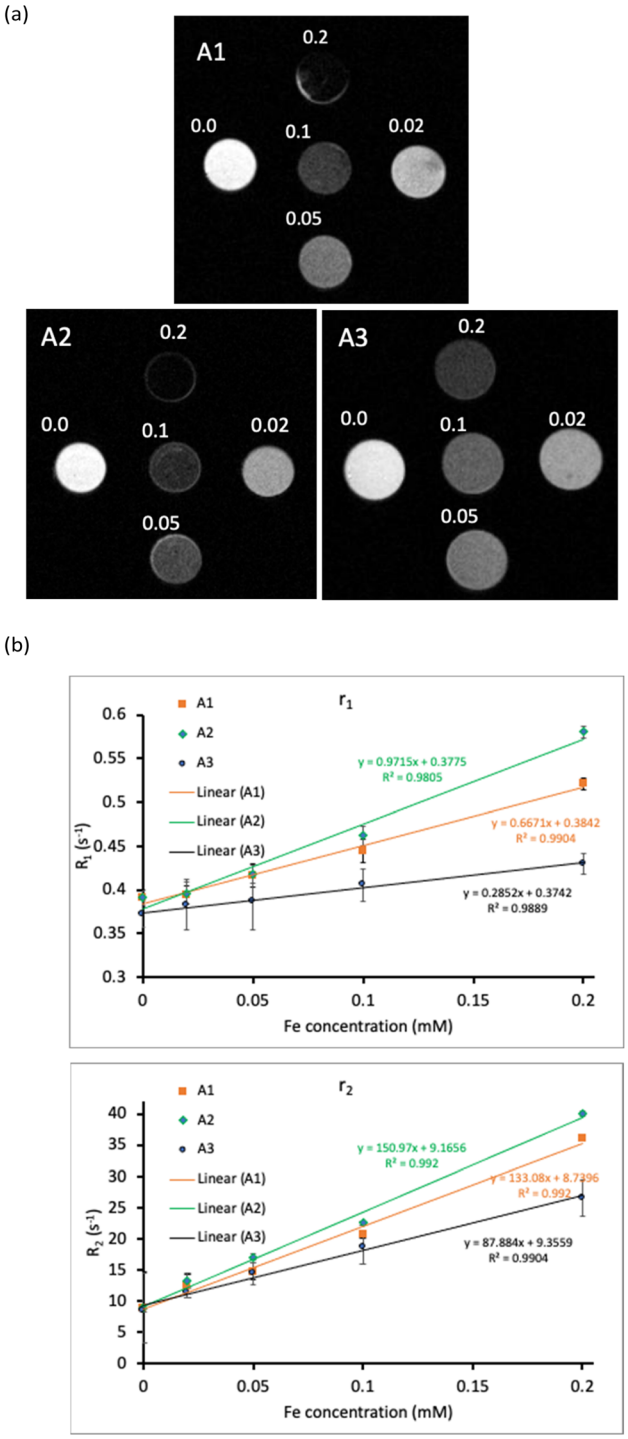

Fig. 5 *In vitro* MRI results: (a) T_2 images of, (b) linear fitting of R_1 and R_2 to Fe concentration.

1 h, 3 h, 6 h and 24 h, the mice were anesthetized with isoflurane (induction: 2% isoflurane in air/oxygen mixture at 1 L min^{-1}; maintenance 0.5–1.5% isoflurane in air/oxygen mixture at 1 L min^{-1}) and imaged with the same photon counter (The Photon IMAGER Optima system, Biospace lab, France) for 2 minutes. After 36 h of injection, the mice were sacrificed, and their organs were collected for further *ex vivo* fluorescent imaging. All acquired images of the whole body of the mice were shown at the same scale. After the acquisition, regions of interest (ROI) were measured to show different fluorescence intensities in signal reception locations.

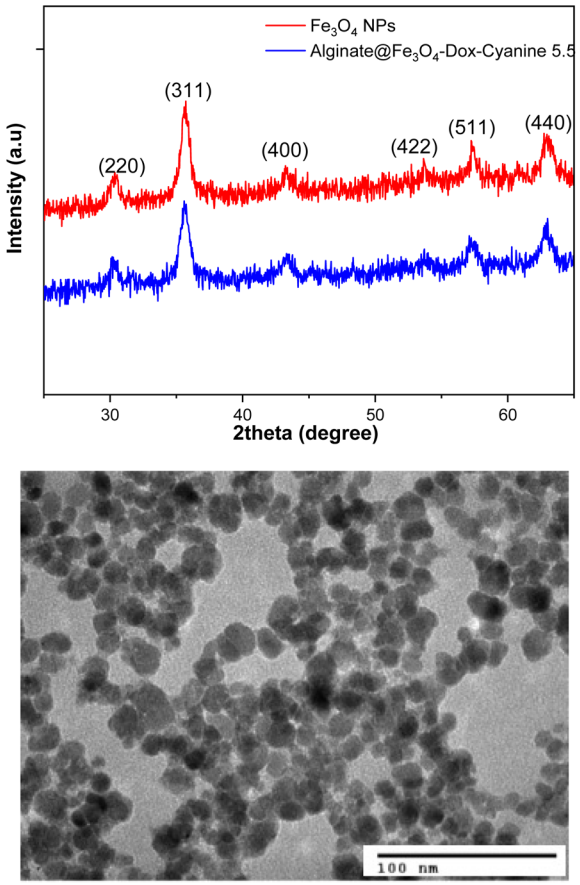

Fig. 6 XRD pattern and TEM image A3.

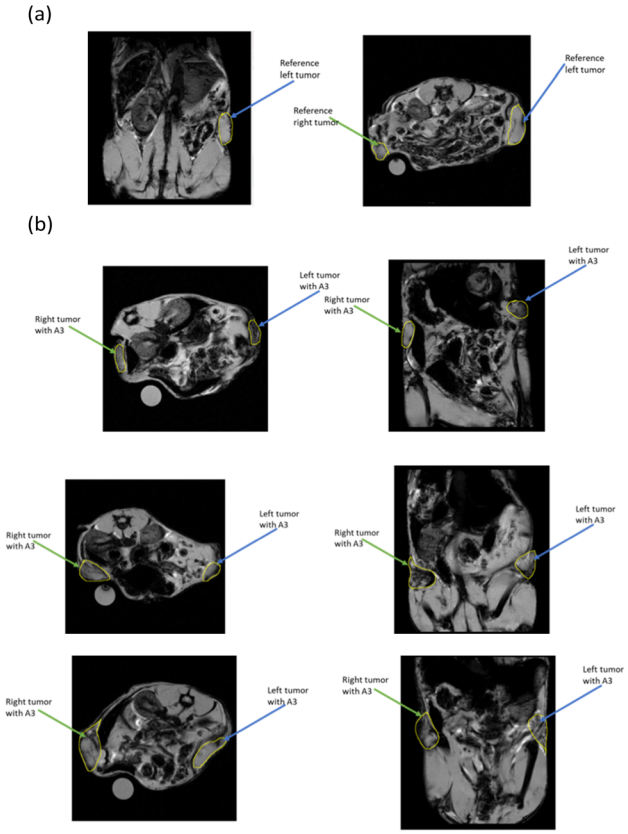

Fig. 7 T_2-Weighted MR images of (a) a control mouse and (b) 3 mice injected with A3.

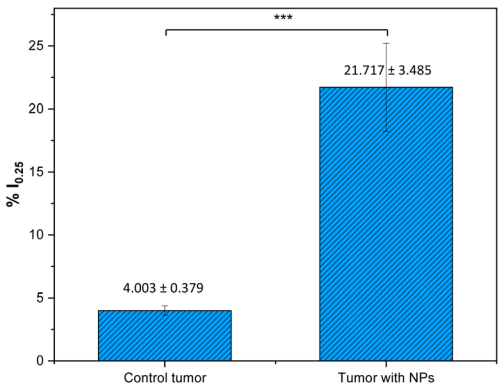

Fig. 8 Percentage of pixels below $I_{0.25}$ of control mice and A3-injected mice (***: different significantly at $p < 0.001$).

2.2.7 ***In vivo* MRI.** The *in vivo* experiments were carried out with T_2-weighted MRI images under the following sequence: FLASH images: Hermitian pulse, TR/TE = 350 ms/5 ms, $\alpha = 40°$, triggered on respiration; field of view of 3 × 3 cm^2, matrix size of 256 × 256 corresponding to 177 μm × 117 μm in-plane resolution, and 15 to 17 slices with a thickness of 1 mm were used, for an acquisition time of about 7 min.

6 Tumor-bearing mice were placed in a 7 T vertical MRI instrument (300WB, Bruker, Avance II, Wissembourg, France) and anesthetized with 1.5% isoflurane in air/O_2 mixture (0.5 L min^{-1} and 0.2 L min^{-1}, respectively). After T_2-weighted MRI imaging before injection, the mice were injected with 150 μL of A3 at the concentration of 25 mM iron through a catheter placed in the tail vein of the animal. The remaining 3 mice were used as controls. T_2-weighted MRI images were acquired 24 h after injection. ParaVision software (version 5.1) was used to process the acquired MRI data. All images were acquired at the same imaging depth to compare the darkening caused by the NPs. The muscle signal was used to normalize the relative signal intensity ratio of nanoparticles in the tumors of nano-injected and control mice.

For the data processing, an MRI image of each slice was opened in the ImageJ software (National Institutes of Health, Bethesda) using the plugin BrukerOpener. The ROI corresponding to the tumor was drawn as equally sized circles (~5 mm in diameter), and the pixel intensity distribution was obtained. The pixel intensity distributions for each slice of the tumor were compiled using MATLAB software (R2023a, Natick, Massachusetts, United States) to obtain a pixel intensity distribution for the whole tumor. The percentage of pixels under the $I_{0.25}$ value was then calculated with the same software by eqn (5):

$$I_{0.25} = 0.25 \times (I_{max} - I_{min}) \quad (5)$$

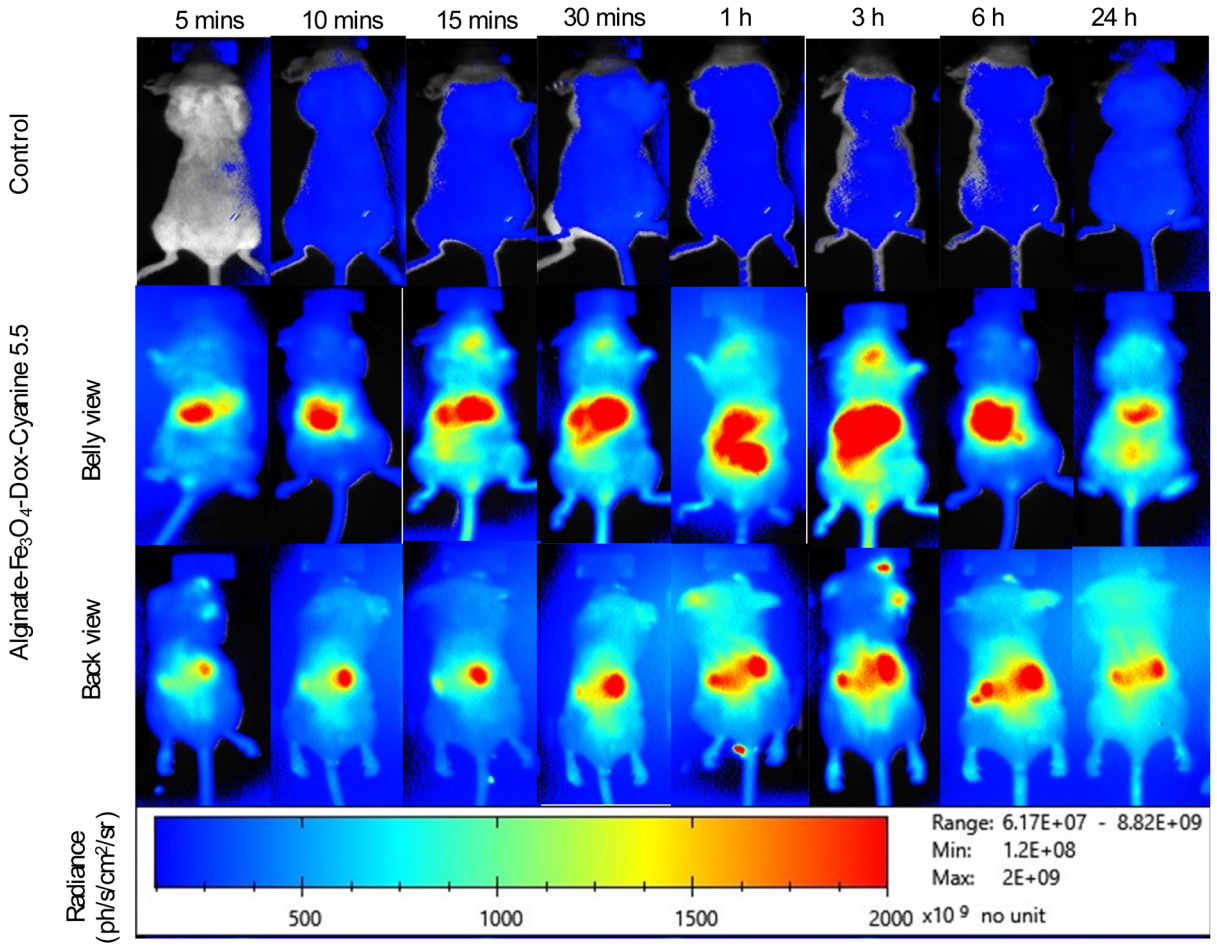

Fig. 9 *In vivo* distribution over time of A3 determined by fluorescence imaging in the representation of the rainbow signal.

In which I_{max} and I_{min} are the maximum and minimum pixel intensity of the intensity distribution histogram.

2.2.8 Statistical analysis. Each experiment was performed in triplicate, and the data are expressed as the mean ± SD. Statistically significant differences were realized at $p < 0.05$ *via* Student's *t*-test. JMP Pro. 13.2 software was used for statistical analysis.

3 Results and discussion

3.1. Size and optical properties

Fig. 1 presents the DLS and Dox EE results of the nanoconjugates. Hydrodynamic sizes of A1 to A4 are from 136 to 210 nm, which belongs to the optimal size range (100–200 nm) of nanoparticles to achieve enhanced permeability and retention effect and escape the filtration of spleen or liver.[29,30] The particle size of the 2-component Fe_3O_4–Dox (A2) is larger than those of other conjugates, even the 3-component A3. This observation can be explained by the fact that in A1 and A3, APTES tightly attachs to Fe_3O_4 NPs and makes the structure of the conjugates more compact.

All four conjugates exhibit highly negative zeta potential, ranging from −32.6 mV to −37.5 mV, implying the high colloidal stability of the conjugates. In this study, alginate was used as a surfactant for the synthesis of the nanoconjugates. Alginate possesses a variety of carboxylate groups that help to maintain the electrostatic repulsion between the NPs.[22] Moreover, the carboxyl groups on the surface of the conjugates make Cyanine 5.5 or DOX combine with other components more tightly.[31] As a result, DOX was efficiently entrapped in the nanoconjugates (Fig. 1c). The encapsulation efficiency (EE%) of A2, A3, and A4 is around 80%. A4 shows a slightly lower EE compared to A2 and A3. This can be due to the role of Fe_3O_4 NPs that could be used as an effective Dox deliverer[25,32,33] in A2 and A3 conjugates.

The UV-Vis and PL spectra of the conjugates are shown in Fig. 2. For the conjugates containing Dox (A2, A3, A4), the absorption of Dox appears at around 500 and 535 nm, and the corresponding emission bands are at 551 and 593 nm. Free Cyanine 5.5 has an absorption maximum of 684 nm and an emission maximum of 710 nm. A1 and A3 show minor redshifts of the NIR peaks in both absorption and emission spectra (690 and 712 nm, respectively). The high intensity of the 712 nm emission peaks confirms that Fe_3O_4 NPs do not interfere with the fluorescence emission of Cyanine 5.5.[12] Fig. 2a shows that at 355 nm, A1 absorbs more than A3 while Fig. 2b shows that it

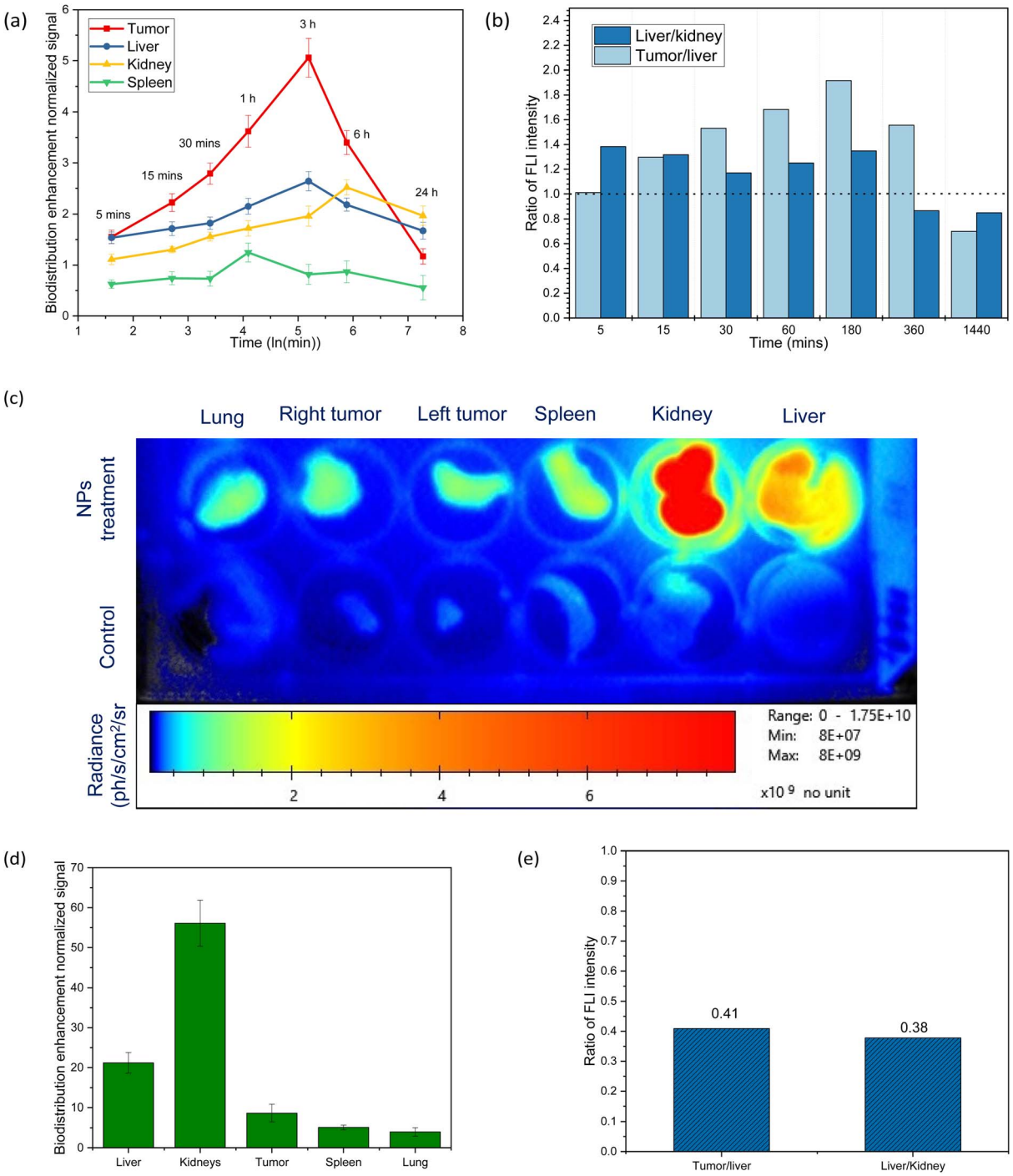

Fig. 10 Signal quantification over time (a and b); *ex vivo* fluorescent images of tumors and other organs (c) and signal quantification at 36 h after injection (d and e).

emits less than A3 (at the same concentration of Cyanine 5.5). This indicates a higher fluorescent efficiency of A3 compared to that of A1 at the near infra-red region (712 nm).[34] On the contrary, A4 shows a broad absorption from around 600 to 750 nm while the emission at the NIR region disappears. This result is in agreement with another report, in which the emission intensity in the NIR region of indocyanine green also decreases with the increase in the concentration of Dox.[35] Notably, A3, a conjugate of Cyanine 5.5 with both fluorescent quenching agent of Fe_3O_4 (ref. 36 and 37) and a high concentration of Dox (5 times to the concentration of Cy 5.5), shows the highest emission intensity. Further calculation of quantum yield for the samples (Fig. 2c) confirms that A3 has the highest quantum yield compared to the other samples. Although there is a small portion of Cyanine 5.5 in A3, the quantum yield of this sample is about $\frac{3}{4}$ of that of pure Cyanine 5.5 (20%, as stated by

the producer Lumiprobe GmbH). This result indicates the potential of A3 in NIR fluorescent imaging.

Table 2 displays the radiance ratio of the conjugates and control (agar) at different excitation/emission wavelengths, and Fig. 3 shows the *in vitro* fluorescent imaging of the conjugates at their optimal excitation/emission wavelength. The radiance of a sample is the number of photons per second that are leaving a square centimeter of the sample tube and radiating into a solid angle of one steradian (ph s^{-1} cm^{-2} sr^{-1}). As shown in Table 2, A2 exhibits the best fluorescent signal at $\lambda_{ex} = 537$ nm and $\lambda_{em} = 597$ nm, while the optimal excitation wavelength of A1, A3, and A4 is 687 nm, and their optimal emission wavelengths vary in the NIR region from 722 to 772 nm (the bold number in the table). The difference in emission wavelengths might relate to the difference in size of the conjugates.[38] The results are also in agreement with the absorption and emission spectra of the conjugates (Fig. 2). Moreover, A3 shows the highest radian ratio, and its red fluorescent signal can be observed at a concentration as low as $C_0/129 = 5 \times 10^{-4}$ mM Cy 5.5 (Fig. 3).

3.2. Magnetic properties

Magnetic properties of Fe_3O_4-containing conjugates (A1, A2, A3) are summarized in Table 3. The saturation magnetization (M_s) and the coercivity (H_c) values of the conjugates were determined by a vibrating magnetometer in the magnetic field of −11000 to 11 000 Oe (Fig. 4a). M_s for A1, A2, and A3 are 63.6, 59.9, and 45.9. emu g^{-1}, respectively. The decrease over the series is consistent with the decrease in the content of Fe_3O_4 present in each conjugate (see Table 1). The small H_c values of A1, A2, and A3 confirm the superparamagnetic properties of these conjugates.[39] The magnetic heating curves (Fig. 4b–d) of the conjugates clearly show that increasing in magnetic field strength (from 100 to 250 Oe) makes the temperature change of the samples increase. Therefore, it is possible to achieve an expected temperature by changing the field strength. The magnetic heating experiments were carried out at room temperature (25–35 °C). In case the temperature of the sample reached the boiling point of water (100 °C), the heating experiment would stop before 1500 s. At the same field strength (100 Oe or 150 Oe), the ΔT_{1500s} of the A1 is higher than that of A2, and the smallest ΔT_{1500s} belongs to A3. At 100 Oe, after 1500 s of magnetic field application, A3 can change the medium's temperature by 25.3 °C. If the starting temperature is the body temperature (37 °C), the temperature can reach over 62 °C, allowing the ablation of tumors by heat.[40] Calculated SAR and ILP values of the conjugates (Table 3) also have the same trend with ΔT_{1500s} because of the decrease in M_s from A1 to A3.[41] Despite having the lowest value, the ILP of A3 (5.1 nH m^2 kg^{-1}) is still higher than many reported Fe_3O_4 NPs.[42–44] Thus, the three conjugates can serve as potential hyperthermia agents.

The ability to enhance the MRI contrast of A1, A2, and A3 was determined by *in vitro* MR images at different iron concentrations taken in T_1-weighted and T_2-weighted modes. Fig. 5a shows the T_2-weighted images of the nanoconjugates. As the Fe concentration increases, the T_2-weighted MR images become darker. The protons of water molecules are affected by the dipole moment of the nanosystems, causing their spin–spin relaxation time (T_2) to decrease. On the other hand, the presence of carboxylate functional groups of alginate causes more water molecules to adsorb on the surface of the nanosystems, also changing the longitudinal relaxation time (T_1).[45] Fig. 5b shows the linear relationship between the relaxation rate ($R_1 = 1/T_1$ and $R_2 = 1/T_2$) and Fe concentration. The slopes of the plots are longitudinal relaxivity (r_1) and transverse relaxivity (r_2) (Table 3). While A2 has the highest r_2 value, A3 shows the highest r_2/r_1 value. Several previous studies also revealed that the presence of Dox[24] or other drug like curcumin can improve the r_2 value.[46] A2 and A3, therefore, can be used as T_2-contrast enhancement agents.

3.3. A3 and its *in vivo* bimodal imaging

Based on the above optical and magnetic properties results, A3 was selected for *in vivo* imaging experiments. Fig. 6 provides some more details of A3. The XRD pattern of A3 shows characteristic peaks at 2θ of 30.1°, 35.4°, 43.1°, 53.4°, 57.0°, 62.6°, corresponding to the (220), (311), (400), (422), (511), and (440) characteristic peaks of Fe_3O_4 NPs.[47] The TEM image shows the core size of A3 is about 10 to 15 nm. The significant difference in the size of A3 measured by TEM (Fig. 6) and by DLS method (Fig. 1a) resulted from the different states of the sample in the 2 measurements. To obtain TEM images, A3 solution was spread in a copper grid and then dried before being applied a high energy electron beam. The electron beam can burn the organic components (alginate, Dox, or Cyanine 5.5), and the image obtained records the size of the Fe_3O_4 core only. In DLS method, the sample was kept in an aqueous medium in which the alginate polymer easily expands and causes the overall hydrodynamic size of the A3 sample much larger than its Fe_3O_4 core. Similar phenomena are also reported elsewhere.[25,48,49]

Fig. 7 displays the *in vivo* MRI images of Balb/C mice with CT26 colon tumors (control and A3-injected mice). The tumor images of A3-injected mice become darker than those of control mice. The dark regions also confirm the dispersion of the A3 conjugate in the tumors (pointed by the arrows) and demonstrate the ability to increase the contrast in MR images with T_2^* weighted mode. This effect allows for a more accurate assessment of the size, shape, and internal structure of the tumor, as well as an easier assessment of the presence or absence of a tumor when it appears inside the body.[50]

To quantify the MRI signal and evaluate the *in vivo* accumulation of the A3 conjugate in tumors, the semi-quantitative method% $I_{0.25}$ was used.[51] Regions of interest (ROIs) were drawn on each slice of the tumor on the MRI image, and the pixel intensity distribution for each slice was obtained. The synthesis of these pixel intensity distribution plots gave a unique pixel intensity distribution for each tumor. Fig. 8 shows that the percentage of pixels below $I_{0.25}$ was significantly different ($p < 0.001$) between control mice and A3-injected mice (4.00 ± 0.38% and 21.72 ± 3.49%, respectively). This reflects the efficient passive accumulation of the nanoconjugate in these tumors.

Fig. 9 shows the *in vivo* distribution of A3 at 5 min, 15 min, 30 min, 1 h, 3 h, 6 h, and 24 h after injection. Immediately after 5 minutes of injection, the fluorescence signal was observed and then increased to reach the maximum at 3 h after injection. After that, the signal was reduced.

The fluorescence signal was then quantitatively analyzed using M3 vision software (BioSpace Lab, France) and expressed as average radiance (ph s^{-1} cm^{-2} sr^{-1}). Regions of interest (ROIs) were drawn around the subcutaneous tumors on both flanks and adjacent tissues to determine the average radiance. The signal was then normalized relative to that of the control mouse to assess the degree of signal enhancement compared to the background (corresponding biological tissue) (Fig. 10a). After 3 hours of injection, the highest signal is obtained in the tumor, followed by the liver, kidney, and spleen. This result is also consistent with the MRI quantitative results above, showing the passive targeting effect of A3 to the tumor site. From 3 h to 24 h, the fluorescence signal at the tumor decreases sharply while the signal intensity at the liver and spleen slightly decreases. The signal at the kidney increases until 6 h after injection, indicating that after 3 h, the nanoconjugate was transferred from tumors to the kidney before clearance.

In addition, the tumor/liver signal ratio, an index of tumor-specific nanoparticle distribution relative to the RES,[52,53] was calculated (Fig. 10b). The tumor/liver signal ratio increases and reaches its highest point at the same time as the highest point of both tumor and liver signal (3 h after injection). This indicates that the conjugate was successful in passively targeting tumors. Further analysis of the liver/kidney signal ratio allowed us to evaluate the role of each organ in the metabolism and excretion of the nanoconjugate.[54] During the first 3 hours, the liver/kidney signal ratio was >1, indicating that the metabolism in the liver was dominant. After 6 and 24 hours of injection, the liver/kidney signal ratio was <1.0, indicating the dominant role of the kidney. In another study, the *in vivo* distribution in a CT26 tumor mouse model of the PEG–BPSi–Cyanine 7.5 nanosystem (size 140 nm) was evaluated. It was shown that after 24 hours, the nanosystem was eliminated mainly through the liver and spleen, followed by fecal excretion.[55] Lyli Mai's research group demonstrated that Cyanine 5.5-conjugated nanobubbles could persist at the tumor site for more than 24 hours in a mouse model of H22 liver tumor. In contrast, free Cyanine 5.5 is rapidly eliminated by renal filtration, followed by urinary excretion.[56]

After 36 hours, the mice were sacrificed, and the tumor, lung, spleen, liver, and kidney were dissected. *Ex vivo* fluorescence imaging (Fig. 10c) was performed to quantify the fluorescence signal in these organs (Fig. 10d and e). The highest fluorescence intensity was in the kidney, followed by the liver and tumor. This result shows that the kidney and liver are the main organs in nanoconjugate elimination. The ratio of tumor/liver signal <0.5 and liver/kidney <0.5 showed that after 36 hours of injection, the nanoconjugate was mainly distributed in the kidney (Fig. 10e) and would be eliminated from the body through the kidney.

4 Conclusion

In conclusion, various conjugates of the three components, Fe_3O_4 NPs, drug (Dox), and dye (Cyanine 5.5), have been prepared based on alginate polymer. Despite containing both fluorescence quenching agents of Fe_3O_4 NPs and Dox, A3 conjugate shows the highest fluorescent intensity in both PL spectra and fluorescence images. A2 (Fe_3O_4–Dox) and A3 (Fe_3O_4–Cy 5.5–Dox) have lower saturate magnetization values but exhibit higher r_2 or r_2/r_1 ratio compared to A1 (Fe_3O_4–Cy 5.5). Selected conjugate A3 was used for *in vivo* MRI and NIR fluorescence imaging. The results confirm that A3 can passively target tumors and enhance MRI contrast. Based on optical images, A3 reaches the maximum concentration at tumors 3 h after injection and then transfers to the kidney for clearance. Thus, the results demonstrate that the A3 conjugate is a promising multifunctional nanoconjugate for *in vivo* MRI and NIR-fluorescence tumor imaging.

Ethical statement

All animal procedures were performed in accordance with the Guidelines for Care and Use of Laboratory Animals of the University of Paris, referral CEEA34 apafis 18.037 and approved by the Animal Ethics Committee No. 34 of the University.

Data availability

All data that support the findings of this study are included in the manuscript.

Author contributions

T. T. H. L.: investigation, writing original draft; review and editing; K. S. P.: investigation, data analysis, review and editing; B. T. D., H. B. H. B., H. N. P., T. D. T. U., Y. W., L. H. D.: investigation; T. T. T. M.: investigation, review and editing; N. Q. T.: investigation, funding acquisition; P. T. H.: conceptualization, funding acquisition, review and editing.

Conflicts of interest

There are no conflicts to declare.

Acknowledgements

This work was funded by the Vietnam Academy of Science and Technology (VAST) under Grant Number NCXS.01.01/23-25.

References

1 F. Bray, M. Laversanne, H. Sung, J. Ferlay, R. L. Siegel, I. Soerjomataram and A. Jemal, *Ca-Cancer J. Clin.*, 2024, **74**, 229–263.

2 E. Atlihan-Gundogdu, D. Ilem-Ozdemir, M. Ekinci, E. Ozgenc, E. S. Demir, B. Sánchez-Dengra and I. González-Alvárez, *J. Pharm. Invest.*, 2020, **50**, 349–361.

3 S. Yoon, S. Y. Cheon, S. Park, D. Lee, Y. Lee, S. Han, M. Kim and H. Koo, *Biomater. Res.*, 2024, **26**, 57.
4 C. Zeng, W. Shang, X. Liang, X. Lieng, Q. Chen, C. Chi, Y. Du, C. Fang and J. Tian, *ACS Appl. Mater. Interfaces*, 2016, **8**, 29232–29241.
5 H. Rui, R. Xing, Z. Xu, Y. Hou, S. Goo and S. Sun, *Adv. Mater.*, 2010, **22**, 2729–2742.
6 H. Gu, S. Fu, Z. Cai and H. Ai, *J. Polym. Sci.*, 2024, **62**, 3103–3121.
7 M. E. Sadat, M. Kaveh Baghbador, A. W. Dunn, H. P. Wagner, R. C. Ewing, J. Zhang, H. Xu, G. M. Pauletti, D. B. Mast and D. Shi, *Appl. Phys. Lett.*, 2014, **105**, 1–6.
8 P. Q. Thong, L. T. Thu Huong, N. D. Tu, H. T. My Nhung, L. Khanh, D. H. Manh, P. H. Nam, N. X. Phuc, J. Alonso, J. Qiao, S. Sridhar, H. P. Thu, M. H. Phan and N. T. Kim Thanh, *Nanomedicine*, 2022, **17**, 1677–1693.
9 G. A. Marcelo, J. Galhano and E. Oliveira, *Dyes Pigm.*, 2023, **208**, 110756.
10 H. Wang, D. N. Udukala, T. N. Samarakoon, M. T. Basel, M. Kalita, G. Abayaweera, H. Manawadu, A. Malalasekera, C. Robinson, D. Villanueva, P. Maynez, L. Bossmann, E. Riedy, J. Barriga, N. Wang, P. Li, D. A. Higgins, G. Zhu, D. L. Troyer and S. H. Bossmann, *Photochem. Photobiol. Sci.*, 2014, **13**, 231–240.
11 K. C. On, J. Rho, H. Y. Yoon, H. Chang, J. Y. Yhee, J. S. Yoon, S. Y. Jeong, H. K. Kim and K. Kim, *Pharmaceutics*, 2020, **12**, 1–14.
12 D. Yoo, C. Lee, B. Seo and Y. Piao, *RSC Adv.*, 2017, **7**, 12876–12885.
13 K. Butowska, A. Woziwodzka, A. Borowik and J. Piosik, *Materials*, 2021, **14**, 1–19.
14 G. Prabha and V. Raj, *Mater. Sci. Eng., C*, 2017, **79**, 410–422.
15 P. I. P. Soares, A. I. Sousa, J. C. Silva, I. M. M. Ferreira, C. M. M. Novo and J. P. Borges, *Carbohydr. Polym.*, 2016, **147**, 304–312.
16 W. Cai, M. Guo, X. Weng, W. Zhang and Z. Chen, *Mater. Sci. Eng., C*, 2019, **98**, 65–73.
17 M. Norouzi, V. Yathindranath, J. A. Thliveris, B. M. Kopec, T. J. Siahaan and D. W. Miller, *Sci. Rep.*, 2020, **10**, 1–18.
18 N. Sadat, H. Motlagh, P. Parvin, F. Ghasemi and F. Atyabi, *Biomed. Opt. Express*, 2016, **7**, 2400–2406.
19 D. Ahn, J. Lee, S. Park, Y. Kwark and K. Y. Lee, *ACS Appl. Mater. Interfaces*, 2014, **6**, 22069–22077.
20 S. Cao, J. Guo, Y. He, M. Alahdal, S. Tang, Y. Zhao, Z. Yang, H. Gao, W. Hu, H. Jiang, L. Qin and L. Jin, *Artif. Cells, Nanomed., Biotechnol.*, 2018, **46**, 642–652.
21 M. A. Taemeh, A. Shiravandi, M. A. Korayem and H. Daemi, *Carbohydr. Polym.*, 2020, **228**, 115419.
22 D. Kothale, U. Verma, N. Dewangan, P. Jana, A. Jain and D. Jain, *Curr. Drug Delivery*, 2020, **17**, 755–775.
23 K. Son Phan, H. Nghi Do, B. Thuy Doan, T. Thu Huong Le, T. Thu Trang Mai, Q. Bao Ngoc Nguyen, T. Nham Dong, B. Hung Bui Ha, V. Dung Dang, L. H. Dang, N. Quyen Tran and P. Thu Ha, *ChemMedChem*, 2024, **20**(5), e202400586.
24 K. Son Phan, B. Thuy Doan, T. Thu Huong Le, T. Thu Trang Mai, T. Dieu Thuy Ung, T. Quang Bui, S. Boumati and P. Thu Ha, *ChemistrySelect*, 2023, **8**(40), e202303580.
25 T. T. H. Le, T. Q. Bui, T. M. T. Ha, M. H. Le, H. N. Pham and P. T. Ha, *J. Mater. Sci.*, 2018, **53**, 13826–13842.
26 H. T. T. Le, K. S. Phan, D. T. T. Ung, L. A. T. Tran, N. T. Dong and T. P. Hà, *Vietnam J. Sci. Technol.*, 2022, **60**, 33–42.
27 K. Lawson-wood, *Fluoresc. Spectrosc.*, 2018, 1–5.
28 T. T. T. Huong, N. T. Loan, L. Van Long, T. D. Phong, T. Ung Thi Dieu and N. Q. Liem, *Opt. Mater.*, 2022, **130**, 112564.
29 J. Wu, *J. Pers. Med.*, 2021, **11**(8), 771.
30 M. Longmire, P. L. Choyke and H. Kobayashi, *Nanomedicine*, 2008, **3**, 703–717.
31 Y. Zhao, S. Tang, J. Guo, M. Alahdal and S. Cao, *Nat. Publ. Gr.*, 2017, **7**, 44758.
32 G. Prabha and V. Raj, *Mater. Sci. Eng., C*, 2017, **79**, 410–422.
33 R. Pashaei-Asl, S. Motaali, E. Ebrahimie, M. Mohammadi-Dehcheshmeh, M. Ebrahimi and M. Pashaeiasl, *Pathol., Res. Pract.*, 2024, 155667.
34 M. Vaishakh and V. P. N. Nampoori, Thermooptic techniques: a tool for interdisciplinary studies, *Photoacoustic and Photothermal Spectroscopy - Principles and Application*, ed. S. N. Thakur, V. N. Rai and J. P. Singh, Elsevier, 2023, ch 8, pp. 185–216.
35 S. Jaiswal, S. B. Dutta, D. Nayak and S. Gupta, *ACS Omega*, 2021, **6**, 34842–34849.
36 Q. Zhang, R. Su, J. P. Wang and Q. Zhang, *J. Nanosci. Nanotechnol.*, 2016, **16**, 7427–7432.
37 C. E. Rivera-Enríquez, M. Ojeda-Martínez, M. E. Cano, V. M. Rentería-Tapia, F. González, H. J. Ojeda Galván and C. Velásquez-Ordoñez, *Ceram. Int.*, 2023, **49**, 41133–41141.
38 Z. Popović, W. Liu, V. P. Chauhan, J. Lee, C. Wong, A. B. Greytak, N. Insin, D. G. Nocera, D. Fukumura, R. K. Jain and M. G. Bawendi, *Angew Chem. Int. Ed. Engl.*, 2010, **49**, 8649–8652.
39 A. K. Singh, O. N. Srivastava and K. Singh, *Nanoscale Res. Lett.*, 2017, **12**, 298.
40 S. K. Sharma, N. Shrivastava, F. Rossi, L. D. Tung and N. T. K. Thanh, *Nano Today*, 2019, **29**, 100795.
41 A. Singh, P. Kumar, S. Pathak, K. Jain, P. Garg, M. Pant, A. K. Mahapatro, D. Rath, L. Wang, S.-K. Kim, K. K. Maurya and R. P. Pant, *J. Alloys Compd.*, 2023, **968**, 171868.
42 A. Hervault, A. E. Dunn, M. Lim, C. Boyer, D. Mott, S. Maenosono and N. T. K. Thanh, *Nanoscale*, 2016, **8**, 12152–12161.
43 B. Dutta, A. Nema, N. G. Shetake, J. Gupta, K. C. Barick, M. A. Lawande, B. N. Pandey, I. K. Priyadarsini and P. A. Hassan, *Mater. Sci. Eng., C*, 2020, **112**, 110915.
44 F. Reyes-Ortega, B. L. Checa Fernández, A. V Delgado and G. R. Iglesias, *Pharmaceutics*, 2019, **11**(10), 517.
45 N. Torkashvand and N. Sarlak, *Eur. Polym. J.*, 2019, **118**, 128–136.
46 M. Ghorbaanee, A. A. Salarian and V. Saba, *J. Inorg. Organomet. Polym. Mater.*, 2018, **28**, 2169–2178.
47 B. Wang, Q. Wei and S. Qu, *Int. J. Electrochem. Sci.*, 2013, **8**, 3786–3793.
48 Y. Ye, J. He, Y. Qiao, Y. Qi, H. Zhang, H. A. Santos, D. Zhong, W. Li, S. Hua, W. Wang, A. Grzybowski, K. Yao and M. Zhou, *Theranostics*, 2020, **10**, 8541–8557.

49 T. M. M. Ways, S. K. Filippov, S. Maji, M. Glassner, M. Cegłowski, R. Hoogenboom, S. King, W. M. Lau and V. V Khutoryanskiy, *J. Colloid Interface Sci.*, 2022, **626**, 251–264.
50 A. Nomani, S. Yousefi, D. Sargsyan and A. Hatefi, *J. Controlled Release*, 2024, **368**, 728–739.
51 C. J. Thébault, G. Ramniceanu, A. Michel, C. Beauvineau, C. Girard, J. Seguin, N. Mignet, C. Ménager and B.-T. Doan, *Mol. Imaging Biol.*, 2019, **21**, 269–278.
52 P. Lebert, M. Adens-Fauquembergue, M. Azahaf, V. Gnemmi, H. Behal, A. Luciani and O. Ernst, *Eur. Radiol.*, 2019, **29**, 5742–5751.
53 Y. Hama and E. Tate, *Br. J. Radiol.*, 2022, **95**, 20211131.
54 B. C. Yung and S. Sostre, *Clin. Nucl. Med.*, 1994, **19**, 228–232.
55 K. Tamarov, J. T. W. Wang, J. Kari, E. Happonen, I. Vesavaara, M. Niemelä, P. Perämäki, K. T. Al-Jamal, W. Xu and V. P. Lehto, *ACS Appl. Mater. Interfaces*, 2021, **13**, 40392–40400.
56 L. Mai, A. Yao, J. Li, Q. Wei, M. Yuchi, X. He, M. Ding and Q. Zhou, *PLoS One*, 2013, **8**, e61224.